A computationally efficient coupled multi-scale model for short fiber reinforced composites

Composites: Part A 163 (2022) 107233

Contents lists available at ScienceDirect

Composites Part A

journal homepage: www.elsevier.com/locate/compositesa

A computationally efficient coupled multi-scale model for short fiber reinforced composites

B.A. Castricum [a,b], M. Fagerström [b], M. Ekh [b], F. Larsson [b], S.M. Mirkhalaf [c,*]

[a] Department of Mechanical Engineering, Eindhoven University of Technology, Eindhoven, The Netherlands
[b] Division of Material and Computational Mechanics, Department of Industrial and Materials Science, Chalmers University of Technology, Gothenburg, Sweden
[c] Department of Physics, University of Gothenburg, Gothenburg, Sweden

ARTICLE INFO

Keywords:
Short fiber reinforced composites
Mechanical behavior
Coupled multi-scale modeling
Orientation averaging
Finite Element Method

ABSTRACT

A coupled multi-scale (macro–micro) model is developed to predict non-linear elasto-plastic behavior of short fiber reinforced composites. At the microscopic level, a recently proposed micro-mechanical model, developed based on a two-step orientation averaging approach, is used. A wide range of micro-structural parameters, including matrix and fiber constitutive parameters, fiber volume fraction and fiber aspect ratio, can be accommodated in the model. Different interactions including Voigt, Reuss and a self-consistent assumption are considered in the model. This micro-mechanical model is then incorporated in a Finite Element model of the macro-scale problem, enabling coupled macro–micro simulations of real-life structures/specimens. Numerical examples and comparisons with experimental data, taken from literature, show that the model gives good predictions. Besides, several strategies and techniques are employed to improve the computational efficiency of the model. These techniques include replacing originally utilized trapezoidal integration (for fiber orientations and calculation of the Eshelby tensor) with more efficient integration schemes, and using a more efficient method for data storage. Comparisons of the computational efforts shows that these improvements substantially decreased the computational cost of the model.

1. Introduction

Short fiber reinforced composites (SFRCs) can be processed rather easily, and complicated geometries can be produced using e.g. injection molding [1]. These materials also have interesting mechanical properties, in comparison to pure polymers. Thus, they are becoming more and more popular for different industries, including the car industry [2,3], which are strongly dependent on numerical simulations in the design processes. As a consequence, it is necessary to have powerful simulation tools, capable of quantitative prediction of the mechanical behavior of SFRCs.

SFRCs have different micro-structural properties which affect their macro-mechanical response [4,5]. As a result, to analyze the general material behavior, it is required to use micro-mechanical models that consider the effect of the micro-structure on the macro-structural behavior in a quantitative and physically-based manner. Micro-mechanical models are typically classified to two categories of mean-field and full-field models. In mean-field models, average quantities are considered in microstructural constituents, and analytical relations are typically obtained for the average response of the whole microstructure. Mean-field models are generally developed using classical mean-field theories such as those by Eshelby [6], Hashin and Shtrikman [7,8], Hill [9], Budiansky [10], and Mori–Tanaka [11], among others. On the other hand, in full-field models also microscopically varying (displacement) fields are accounted for. In these models, equilibrium equations are solved using different numerical techniques such as Finite Element Method (FEM) [12–15] or Fast Fourier Transform (FFT) [16,17].

With different kinds of micro-mechanical models, it is possible to obtain the behavior of different materials (see e.g. [18–22]) at a *single material point*. However, to analyze a *full-scale structure/specimen*, multi-scale models are required, where coupled macro–micro simulations are conducted simultaneously and in a nested fashion. The modeling approach considers the stress–strain relationship at each macroscopic point as the relation between the homogenized stress (volume averaged over a micro-mechanical material sample) and the macroscopic strain at the particular macroscale location (applied to the micro-mechanical model).

A large number of coupled multi-scale models are developed for different kind of materials and different applications (see e.g. [23–25]). In fact, multi-scale modeling is quite relevant for SFRCs, the manufacturing (e.g. through injection molding) often results in a varying

* Corresponding author.
E-mail address: mohsen.mirkhalaf@physics.gu.se (S.M. Mirkhalaf).

https://doi.org/10.1016/j.compositesa.2022.107233
Received 14 June 2022; Received in revised form 1 September 2022; Accepted 26 September 2022
Available online 12 October 2022

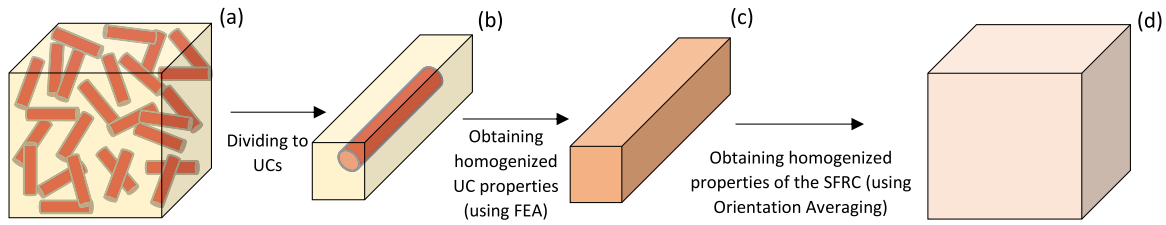

Fig. 1. Schematic representation of the micro-mechanical model used in this study [5].

fiber orientation distribution throughout one and the same part. Points closer to the mold surface get a more aligned orientation with the flow direction (see e.g. [26,27]). As it gets further away from the mold surface, fibers have a less preferred orientation with the flow.

In this study, a coupled multi-scale model, combining FEM (at the macro-level) and a micro-mechanical model (at the micro-level) is developed for short fiber reinforced composites. The FEM package PyFEM presented by de Borst et al. [28] is used for the macroscopic scale, and the micro-mechanical model proposed by Mirkhalaf et al. [20] is used at the microscopic scale. In the micro-mechanical model, three global–local interaction assumptions are used, namely Voigt, Reuss and self-consistent assumptions. In order to improve the computational efficiency of the model, the originally utilized trapezoidal integration scheme, for orientation distribution, is replaced with the *Bazant scheme* [29] which results is considerable improvement of the model efficiency and computations time. Also, the computational cost of the calculation of the Eshelby tensor (for the self-consistent interaction) is considerably reduced by employing an efficient scheme developed by Mengmeng et al. [30]. Moreover, a new strategy for data storage is adopted which decreases the required memory for heavy simulations. With the proposed model, it is possible to have computationally efficient full-scale analysis of structures/specimens (manufactured from short fiber reinforced composites) while considering a variety of micro-structural properties.

The remainder of this paper is structured as follows. Section 2 explains very briefly the micro-mechanical model used in this study. Section 3 details the proposed coupled multi-scale model. The computational efficiency of the model is also investigated in Section 3. Section 4 describes the adopted techniques to make the model computationally efficient. Results, obtained with the proposed model, and discussions are given in Section 5. Finally, Section 6 summarizes the output of this study and gives some concluding remarks.

2. Micro-mechanical model

In this section, the micro-mechanical model developed by Mirkhalaf et al. [20], used at the microscopic level of the proposed model, is briefly explained. The model is developed on an Orientation Averaging platform, based on the study by Advani and Tucker [31]. Two configurations are distinguished: a global configuration at the composite level, and a local configuration at the UC level. These two configuration are related by a transformation (rotation):

$$\mathbf{e}_i^L = \mathbf{R} \cdot \mathbf{e}_i, \tag{1}$$

where, $\mathbf{e}_i$ and $\mathbf{e}_i^L$ represent the global and local orthonormal base vectors, respectively. A schematic representation of the model is shown in Fig. 1. In this model, There are two homogenization steps which are described in Sections 2.2 and 2.3. Before performing these two homogenization steps, it is needed to define a global–local interaction in order to obtain the strain state of each UC as a function of composite strain state. These interactions are explained briefly in Section 2.1.

2.1. Interaction assumptions

In this study, three global–local interactions, including Voigt (uniform strain), Reuss (uniform stress) and self-consistent assumptions are considered.

2.1.1. Voigt interaction

Based on this assumption, all UCs experience the same strain at the global configuration which is equivalent to the composite strain:

$$\Delta\boldsymbol{\varepsilon}_{\mathrm{U}} = \Delta\boldsymbol{\varepsilon}_{\mathrm{C}}, \tag{2}$$

where $\Delta\boldsymbol{\varepsilon}_{\mathrm{U}}$ and $\Delta\boldsymbol{\varepsilon}_{\mathrm{C}}$ represent the incremental UC strain at the global configuration and the incremental composite strain, respectively. The local components of the strain increment for each UC is obtained by

$$\Delta\boldsymbol{\varepsilon}_U^L = \mathbf{R}(\mathbf{p}) \cdot \Delta\boldsymbol{\varepsilon}_C \cdot \mathbf{R}^T(\mathbf{p}) = \left[\mathbf{R}(\mathbf{p}) \,\overline{\otimes}\, \mathbf{R}(\mathbf{p})\right] : \Delta\boldsymbol{\varepsilon}_C. \tag{3}$$

The Voigt assumption results in the upper bound prediction of stiffness.

2.1.2. Reuss interaction

The Reuss interaction implies that all UCs experience the same stress:

$$\boldsymbol{\sigma}_U = \boldsymbol{\sigma}_C. \tag{4}$$

As a result, the local components of the UC stress are obtained by

$$\Delta\boldsymbol{\sigma}_U^L = \mathbf{R}(\mathbf{p}) \cdot \Delta\boldsymbol{\sigma}_U \cdot \mathbf{R}^T(\mathbf{p}) = \left[\mathbf{R}(\mathbf{p}) \,\overline{\otimes}\, \mathbf{R}(\mathbf{p})\right] : \Delta\boldsymbol{\sigma}_U. \tag{5}$$

The incremental local components of the UC strain are then given by

$$\Delta\boldsymbol{\varepsilon}_U^L = (\mathbb{C}_U^L)^{-1} : \Delta\boldsymbol{\sigma}_U^L, \tag{6}$$

where $\mathbb{C}_U^L$ is the UC stiffness tensor at the local coordinate system. The Reuss assumption results in the lower bound of stiffness prediction.

2.1.3. Self-consistent interaction

The Voigt and Reuss interactions are strong assumption which may result in unrealistic predictions. This is partially due to the fact that interaction between neighboring fibers is neglected in these assumptions. Therefore, a self-consistent interaction is also developed in which fiber interactions are implicitly taken into account. Using this assumption implies that each of the unit cells is embedded in an *equivalent homogeneous medium*. Using the self-consistent interaction, the UC incremental strain is obtained by

$$\Delta\boldsymbol{\varepsilon}_U = \left[\mathbb{I} + \mathbb{E} : \left(\left[\mathbb{C}_C^{SC}\right]^{-1} : \mathbb{C}_U - \mathbb{I}\right)\right]^{-1} : \Delta\boldsymbol{\varepsilon}_C, \tag{7}$$

where $\mathbb{I}$ is the fourth order identity tensor, $\mathbb{E}$ is the fourth order Eshelby tensor which is a function of stiffness tensor, $\mathbb{C}_C^{SC}$ is the composite stiffness tensor using the self-consistent assumption, and $\mathbb{C}_U$ is the UC stiffness tensor at the global coordinate system. We note that, in order to facilitate the analytical evaluation of the Eshelby tensor, the effective medium representing the UC is considered uniform inside an ellipsoid inclusion embedded in the globally effective (homogenized) composite. The resulting composite stiffness tensor is given by

$$\mathbb{C}_C^{SC} = \oint \mathbb{C}_U : \left[\mathbb{I} + \mathbb{E} : \left(\left[\mathbb{C}_C^{SC}\right]^{-1} : \mathbb{C}_U - \mathbb{I}\right)\right]^{-1} \psi(\mathbf{p})\mathrm{d}\mathbf{p}. \tag{8}$$

It should be noted that there is no explicit solution for Eq. (8) and an iterative procedure is used to solve the equation. Once the composite stiffness is obtained, the UC incremental strain is calculated using Eq. (7), and then, the local incremental UC strain is given by

$$\Delta\boldsymbol{\varepsilon}_U^L = \mathbf{R}(\mathbf{p}) \cdot \Delta\boldsymbol{\varepsilon}_U \cdot \mathbf{R}^T(\mathbf{p}) = \left[\mathbf{R}(\mathbf{p}) \,\overline{\otimes}\, \mathbf{R}(\mathbf{p})\right] : \Delta\boldsymbol{\varepsilon}_U. \tag{9}$$

For more details about the self-consistent interaction, an interested reader is referred to [5].

2.2. First homogenization step

First a Unit Cell (UC) including a single fiber surrounded by the matrix material is defined. The homogenized properties of the UC is obtained using Finite Element Analysis ((b) to (c) in Fig. 1). Then, a surrogate constitutive model is calibrated using applied strain - homogenized stress data from FEA conducted on the UC.

In particular, the surrogate model is an elasto-plastic model with simplified transverse isotropy for both elasticity and Hill's yield criterion. The linear elastic stiffness tensor of the material model is given by

$$\mathbb{C}_U^{\mathrm{e}} = \mathbb{C}_U^{\mathrm{e,iso}} + (C-1)(2G+L)\,\mathbf{A} \quad \text{with } \mathbb{C}_U^{\mathrm{e,iso}} = 2G\mathbb{I} + L(\mathbf{I}\otimes\mathbf{I}) \quad \text{and } \mathbf{A} = \mathbf{p}\otimes\mathbf{p}, \tag{10}$$

where the tensor $\mathbb{C}_U^{\mathrm{e,iso}}$ represents the isotropic linear elasticity stiffness tensor, the scalars G and L are the Lamé parameters, and the parameter C is the additional parameter (compared to standard isotropic elasticity) which characterizes the reduced transverse isotropic elasticity. The second and fourth order identity tensors are represented by $\mathbf{I}$ and $\mathbb{I}$, respectively. The fiber orientation is given by $\mathbf{p}$ which is defined using two angles in a spherical coordinate system [31].

Furthermore, following [32,33], a mean-stress independent transversely isotropic version of Hill's yield function is used as

$$\Phi_U(\mathbf{s}_U, \bar{\varepsilon}_U^p) = \mathbf{s}_U : \mathbb{G}_U : \mathbf{s}_U - \alpha\left(\bar{\varepsilon}_U^p\right), \tag{11}$$

where, $\mathbf{s}_U$ is the deviatoric stress tensor, $\alpha\left(\bar{\varepsilon}_U^p\right)$ is an isotropic hardening function, and the fourth order tensor $\mathbb{G}_U$ is defined by

$$\mathbb{G}_U = (A+2B)\mathbb{I} + (5A+B-2F)\mathbf{A}\otimes\mathbf{A} + (F-A-2B)\left[\mathbf{I}\,\overline{\otimes}\,\mathbf{A} + \mathbf{A}\,\overline{\otimes}\,\mathbf{I}\right]. \tag{12}$$

The operator $\overline{\otimes}$ represents a non-standard open product.[1] Parameters A, B and F are dependent on the normal and shear yield stresses of the UC (see more details in [20]). The isotropic hardening function $\alpha(\bar{\varepsilon}^p)$ is assumed to be non-linear and given by

$$\alpha(\bar{\varepsilon}_U^p) = 1 + H_1\bar{\varepsilon}_U^p + H_2(\bar{\varepsilon}_U^p)^2 + H_3(\bar{\varepsilon}_U^p)^3, \tag{13}$$

where $\bar{\varepsilon}_U^p$ is the accumulated effective plastic strain and H_1, H_2 and H_3 represent the hardening parameters.

Remark 1. In this work, plasticity is considered as the driving mechanism of non-linearity, and other phenomena such as matrix-fiber debonding are not considered. Interfacial debonding can in principle be included in the finite element simulations using a cohesive zone interface. In that case, it will most likely be required to extend the surrogate model so that the model can capture this damage mechanism properly.

2.3. Second homogenization step

In the second step ((c) to (d) in Fig. 1), the composite homogenized properties are obtained considering the orientation distribution of fibers and using the UC homogenized properties approximated by the elasto-plastic surrogate model. In this process, two coordinate systems are considered: a global coordinate system at the composite level, and a local coordinate system at the UC level. The orthonormal base vectors for these systems $\mathbf{e}_i$ and $\mathbf{e}_i^L$ define the coordinate system transformation matrix $\mathbf{R}$:

$$R_{ij} = \mathbf{e}_i^L \cdot \mathbf{e}_i, \tag{14}$$

[1] The index notation for the non-standard open product ($\overline{\otimes}$) is given by $(\mathbf{A}\overline{\otimes}\mathbf{B})_{ijkl} = A_{ik}B_{jl}$.

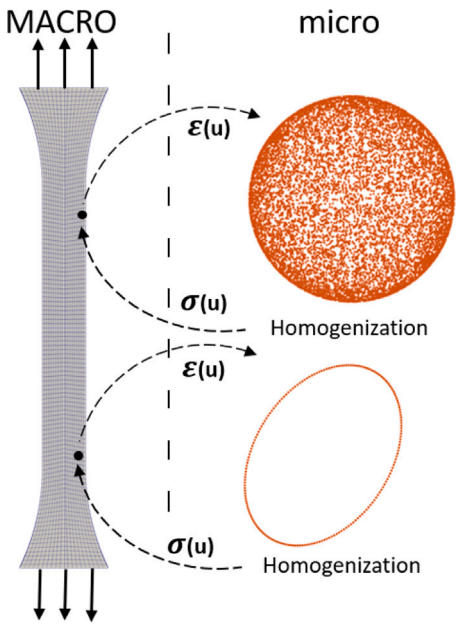

Fig. 2. Schematic representation of the coupled multi-scale model.

The composite stress at each macroscopic location is computed in an incremental fashion. Thus, the stress at a new time instance is given by an incremental update of the stress from the previous time instance. To derive the incremental update, we start by noting that we can obtain the stress of each UC (in the local coordinate system and using the surrogate model). The UC stress components at the global coordinate system are then given by

$$\boldsymbol{\sigma}_U = \mathbf{R}^T\{\mathbf{p}\}\cdot\boldsymbol{\sigma}_U^L\cdot\mathbf{R}\{\mathbf{p}\} = \left[\mathbf{R}^T\{\mathbf{p}\}\,\overline{\otimes}\,\mathbf{R}^T\{\mathbf{p}\}\right] : \boldsymbol{\sigma}_U^L, \tag{15}$$

where $\mathbf{p}$ is a unit vector representing the fiber orientation. To obtain the total composite stress, volume averaging of the UC stress over the volume of the RVE is performed:

$$\boldsymbol{\sigma}_C = \int_\Omega \left[\mathbf{R}^T\{\mathbf{p}\}\,\overline{\otimes}\,\mathbf{R}^T\{\mathbf{p}\}\right] : \boldsymbol{\sigma}_U^L\ \psi\{\mathbf{p}\}d\mathbf{p}, \tag{16}$$

where $\psi\{\mathbf{p}\}$ is the probability distribution function of orientation [31]. With Eq. (16), the components of the composite stress at the global coordinate system are defined. However, as we seek to result in an incremental updating scheme of the stress, we consider the time derivative of Eq. (16) under the assumption that no rotation of fibers occur during deformation, whereby the stress-rate is obtained as:

$$\dot{\boldsymbol{\sigma}}_C = \int_\Omega \left[\mathbf{R}^T(\mathbf{p})\,\overline{\otimes}\,\mathbf{R}^T(\mathbf{p})\right] : \dot{\boldsymbol{\sigma}}_U^L\ \psi(\mathbf{p})\mathrm{d}\mathbf{p}. \tag{17}$$

Thus, the incremental stress reads:

$$\Delta\boldsymbol{\sigma}_C = \int_\Omega \left[\mathbf{R}^T(\mathbf{p})\,\overline{\otimes}\,\mathbf{R}^T(\mathbf{p})\right] : \Delta\boldsymbol{\sigma}_U^L\ \psi(\mathbf{p})\mathrm{d}\mathbf{p}, \tag{18}$$

where $\Delta\boldsymbol{\sigma}_U^L$ is the incremental UC stress at the local configuration.

For a more elaborated discussion on the micro-mechanical model and its implementation in an incremental framework, the reader is referred to Mirkhalaf et al. [20].

3. Coupled multi-scale model

In this section, the proposed coupled multi-scale model is explained and the computational efficiency of the model is investigated.

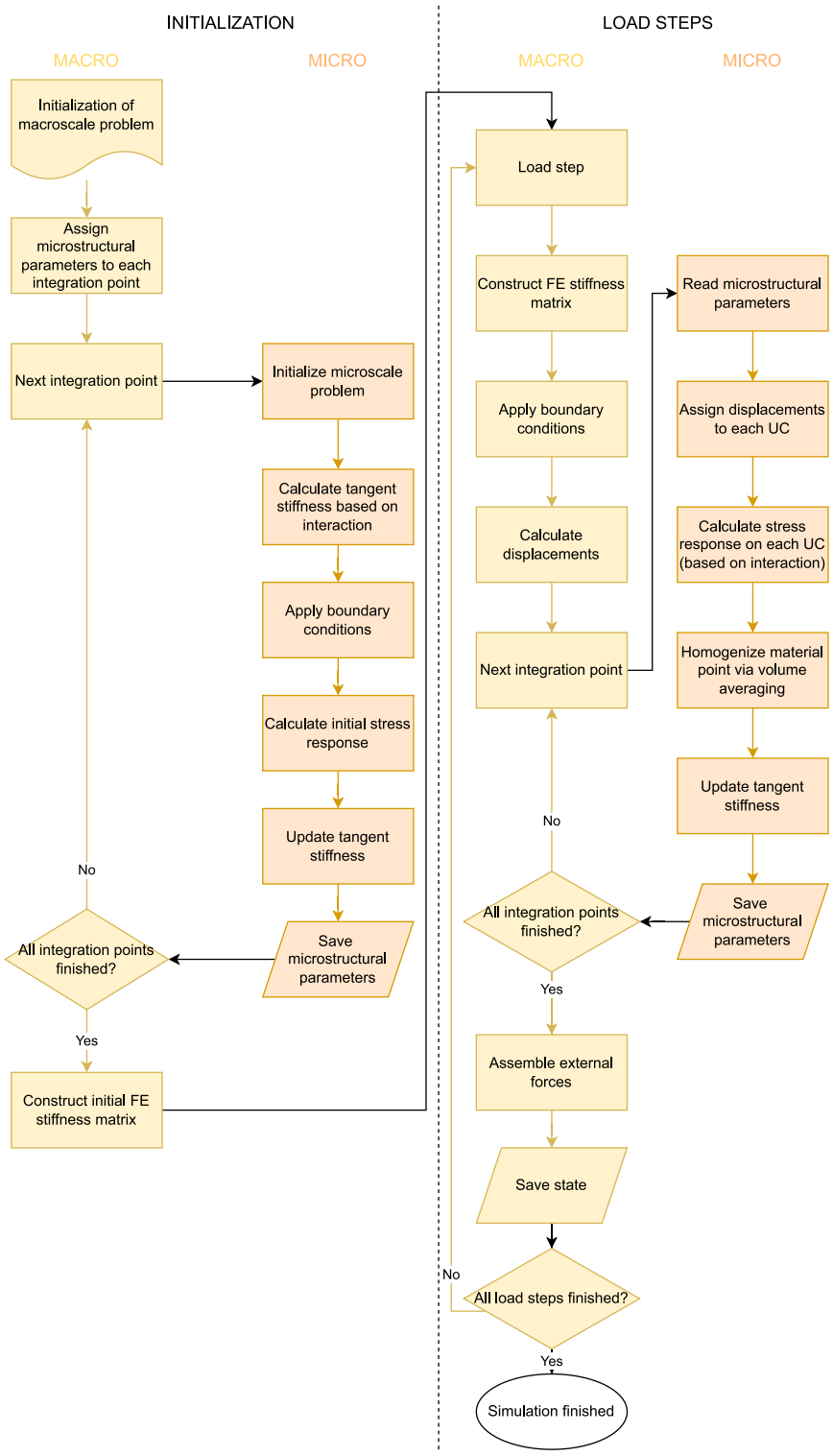

Fig. 3. Flow chart of the implementation of the coupled model.

3.1. Coupling

In the coupled multi-scale model, the constitutive behavior of each macroscopic point (each integration point in the FE context), is determined by the micro-mechanical model (instead of by a conventional continuum constitutive law). Fig. 2 shows a schematic figure representing the coupled multi-scale model. First, the macroscopic model is constructed based on a user-supplied mesh file. In this mesh file, the node coordinates, the element connectivities, and the boundary conditions are described. Then, the micro-mechanical parameters including fiber orientation distribution, interaction assumption (Voigt, Reuss or self-consistent) and the material properties for the surrogate constitutive model (representing the macroscale mode UC response), are given to the model. Now that all required information are available, the macroscopic strain (strain at each FE integration point) is calculated

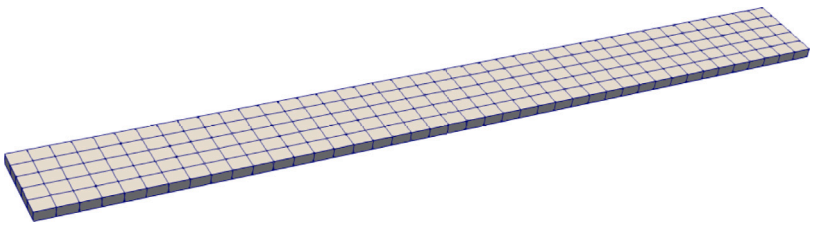

Fig. 4. Finite element mesh of the coupled multi-scale simulations on a polypropylene/flax SFRC.

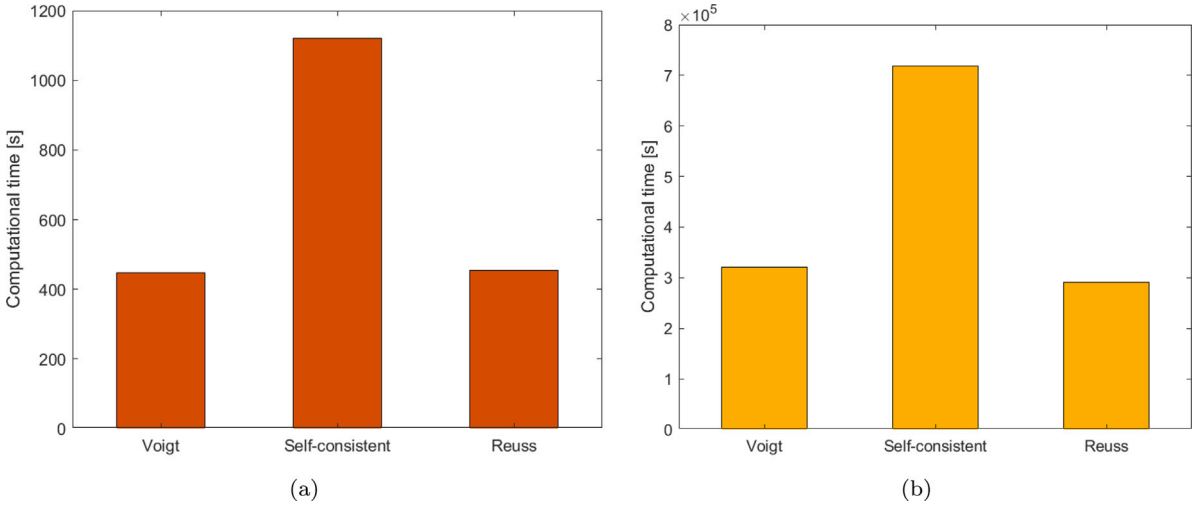

Fig. 5. Calculation time of (a): micro-mechanical simulations with the different interactions for a Polyamide/glass SFRC, and (b): coupled multi-scale simulations with different interactions for a polypropylene/flax SFRC.

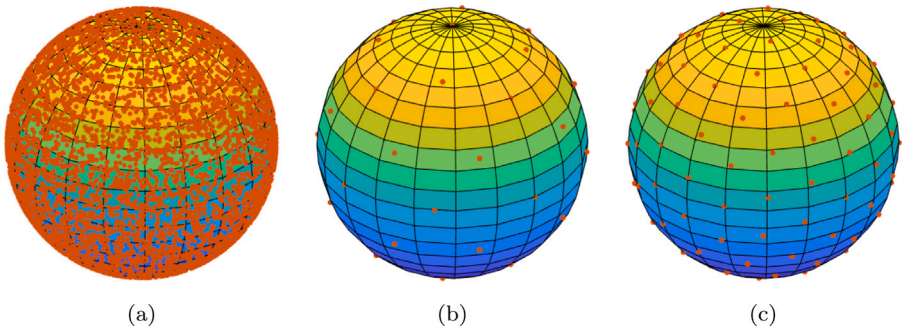

Fig. 6. Visualization of integration points on a unit sphere, (a): 5000 random orientations on the unit sphere, (b): Bazant 21 × 2 scheme points on the unit sphere, (c): Bazant 61 × 2 scheme points on the unit cell.

by the FE formulations and is passed to the micro-mechanical model. Then, the microscopic strain (each UC strain) is determined using the macroscopic strain and based on the interaction assumption. Once the microscopic strain is known for each UC, the UC stress is calculated using the surrogate constitutive model. Next, the micro-mechanical model homogenizes the stresses (obtained for all UCs) and returns this stress tensor (macroscopic stress at the integration point) to the macroscale. The FEM code goes to the next integration point and the same procedure is followed. Fig. 3 shows a flow chart representing different steps of the coupled multi-scale model.

Remark 2. The Finite Element equations are solved with an explicit time-stepping algorithm. The advantages of using such a solver instead of an implicit solver for non-linear problems are that no iterations are needed (with e.g., Newton–Raphson technique) and that difficulties to achieve convergence are circumvented. The drawback is that more time-steps are needed.

3.2. Investigating computational cost of the model

In this section, the computational efficiency of both the micro-mechanical model, and more importantly, the coupled multi-scale model are investigated. Micro-mechanical simulations are performed for a Polyamide matrix composite reinforced with short glass fibers, considering 5000 randomly distributed fibers (unit cells). This material is explained more detailed in Section 5. A uniaxial strain of 1.75% is imposed in 175 load increment.

Also, the computational cost of the coupled model is investigated using a Polypropylene matrix composite reinforced with flax fibers. For each macroscopic integration point, again the same number of fibers and the same orientation of the fibers are considered. This material is also explained in Section 5. The FE mesh of the analyzed sample is shown in Fig. 4.

The dimensions of the FE model are: length = 125 mm, width = 12.5 mm, thickness = 1.5 mm. The original sample size is length =

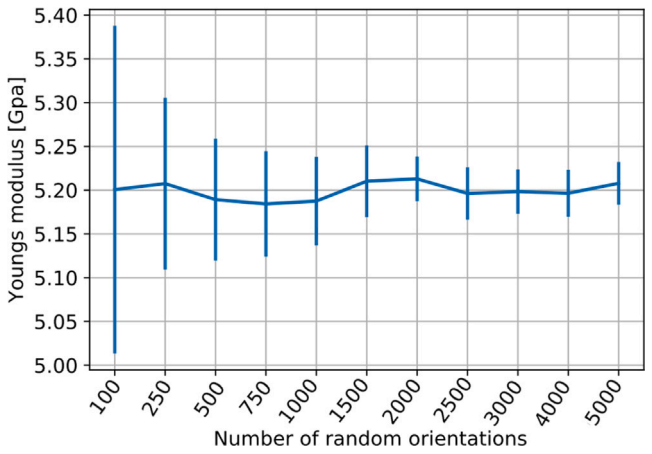

Fig. 7. Young's modulus and its standard deviation for different number of random orientated fibers.

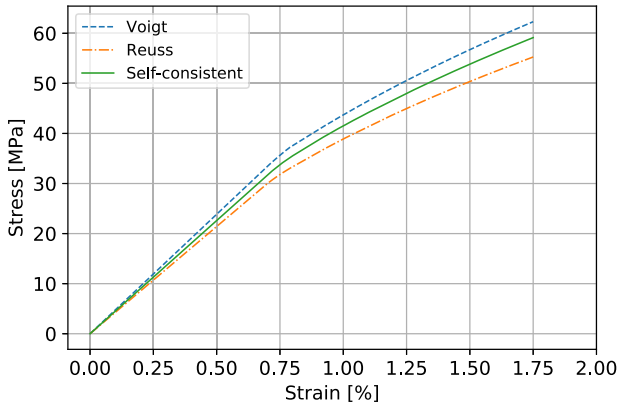

Fig. 8. Micro-mechanical stress–strain curves for the polyamide/glass SFRC with different interaction assumption.

250 mm, width = 25 mm, thickness = 3 mm [36], but due to the symmetric loading conditions, it suffices to only model one eighth of the sample. The sample is spatially discretized with 210 3D solid elements with 8 integration points. A macroscopic strain of 2% is applied in 40 load increments. Fig. 5 shows the calculation time for the aforementioned simulations.

4. Improving computational efficiency of the model

As it was shown in Section 3.2, conducting simulations, particularly using the coupled model, are computationally heavy. Hence, in this study, some techniques are employed to improve the computational efficiency of the model. In the micro-mechanical model, two integrations are carried out: (i) over the fibers orientation distribution, and (ii) for calculation of the Eshelby tensor. Performing these computational integrals make the coupled multi-scale model very heavy. In the followings, more efficient approaches are described to replace the original integration schemes.

4.1. Improving the speed of integrations

Several authors have used the integration approach developed by Bazant et al. [29] for predictions of material behavior (see e.g [37–40]). Hereafter, this approach is referred to as the *Bazant scheme*. The Bazant scheme evaluates the integral on the unit sphere to a summation of the integrand evaluated at specific points multiplied with associated weights (similar to the Gauss quadrature). These points are determined by dividing the surface into polyhedral elements with a high degree of symmetry and individual areas ΔA_i, and then calculating the centroid of these element areas. The points used in the scheme are the centroid points together with points which lay on the edges of the element areas. Some combinations of points are symmetric to all three coordinate planes, this combination of points are used in the so-called orthogonal scheme. In the proposed model in this study, three Bazant schemes will be used: (I): Bazant 21 × 2 orthogonal scheme, (II): Bazant 21 × 2 scheme, (III): Bazant 61 × 2 scheme. These schemes replace the random orientated points by 42 or 122 specifically placed points over unit sphere. In Fig. 6, 5000 random points and the Bazant 21 × 2 scheme can be seen. It should be noted that, using fewer number of orientations not only reduces dramatically the amount of required calculations, but also helps for storage of internal variables. For each fiber, the local stresses, local strains, local stiffness tensor, the rotation tensor, and the plastic strains are needed to be stored. When fewer fibers are used, the memory required to store the internal variables becomes significantly lower, which makes the model more efficient.

4.2. Improving the speed of Eshelby tensor computations

In the micro-mechanical model, for using the self-consistent interaction, it is required to calculate the Eshelby tensor (see [5,20]). To obtain this Eshelby tensor, an integral over the unit sphere is performed, which is computationally expensive. Mengmeng et al. [30] developed an efficient and optimal scheme for the numerical evaluation of this Eshelby tensor based on the dimension of the inclusion. In this study, the Eshelby tensor formulation uses an aspect ratio of a unit sphere which is not necessarily the most appropriate choice. However, it should be emphasized that the actual UC aspect ratio was already considered in the computational homogenization simulations to obtain the UC homogenized response. For the case of unit aspect ratio, the model derived by Mengmeng et al. [30] advises evaluating the integration over the unit sphere via the Lebedev 974 point scheme [41]. The Lebedev quadature is similar to the Bazant scheme. The grid points are derived in such a way that they lie on the surface of the sphere and to be invariant under the octahedral rotation group with inversion. Depending on the order of the Lebedev scheme, a combination of points is chosen and used in this scheme.

In this work, an Eshelby tensor for anisotropic medium, first developed by Lebensohn et al. [42], is used. In this tensor, the fourth order stiffness tensor is related to the Eshelby tensor via an auxiliary tensor. The auxiliary tensor $\mathbb{T}$ is obtained by evaluating the integral:

$$\mathbb{T} = \frac{a_1 a_2 a_3}{4\pi} \int_0^{2\pi} \left\{ \int_0^{\pi} \mathbb{F}(\theta, \phi) \sin\phi d\phi \right\} d\theta \tag{19}$$

Here, θ and ϕ are spherical angles on the unit sphere. Currently, the integral is solved with the trapezoidal rule where the sphere is split into 7200 points and numerically evaluated. A more computational efficient method of solving this equation is using the Lebedev quadrature. The auxiliary tensor $\mathbb{T}$ can be solved via the Lebedev quadrature as:

$$\mathbb{T}_{ijkl} = a_1 a_2 a_3 \sum_{p=1}^{N} w_p [f(\theta_p, \phi_p)]_{ijkl}, \tag{20}$$

where a_1, a_2 and a_3 are the dimension of the inclusion, p is the point on the unit sphere, N is the total amount of points, w_p is the weight corresponding to point p and θ and ϕ are the angles describing the point. The function $F(\theta, \phi)$ relates the homogenized UC behavior to the ellipse as:

$$[F(\theta_p, \phi_p)]_{ijkl} = \frac{z_j z_l A_{ik}}{[(a_1 z_1)^2 + (a_2 z_2)^2 + (a_3 z_3)^2]^{3/2}}, \tag{21}$$

where A is a tensor relating the homogenized UC material properties to the inclusion and z is a vector describing the angles of the point:

$$z = \begin{bmatrix} \cos\theta \sin\phi \\ \sin\theta \cos\phi \\ \cos\theta \end{bmatrix}. \tag{22}$$

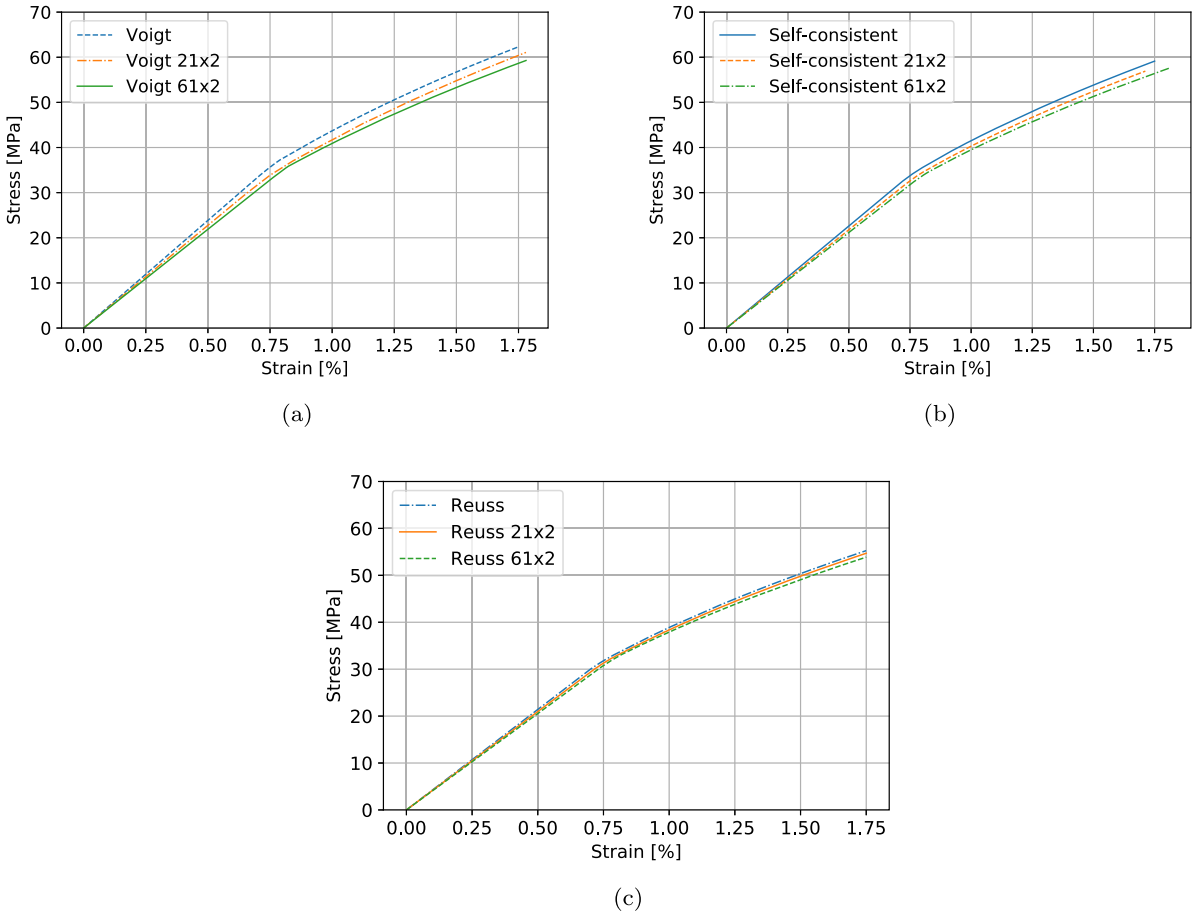

Fig. 9. Stress–strain curve of the micro-mechanical response with 5000 random orientations, Bazant 21 × 2 scheme and Bazant 61 × 2 scheme for, (a): Voigt interaction, (b): Self-consistent interaction, (c): Reuss interaction.

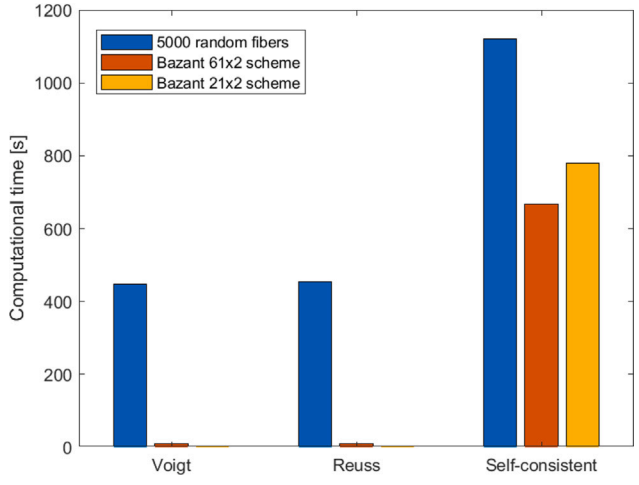

Fig. 10. Computational time of the micro-mechanical model for 5000 random fibers, Bazant 61 × 2 scheme and Bazant 21 × 2 scheme.

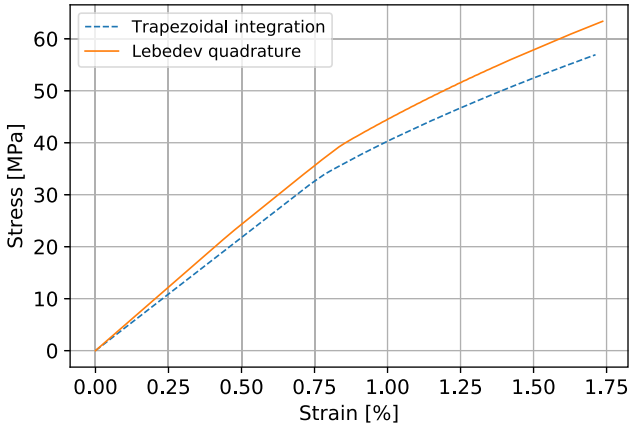

Fig. 11. Comparison of the evaluation of the Eshelby tensor in the self-consistent interaction with the Lebedev quadrature and the trapezoidal scheme.

Eq. (20) is evaluated as follows:

$$T_{ijkl} = a_1 a_2 a_3 \{ w(A^1) \sum_{p=1}^{6} [F(A_p^1)]_{ijkl} + w(A^2) \sum_{p=1}^{12} [F(A_p^2)]_{ijkl} + w(A^3) \sum_{p=1}^{8} [F(A_p^3)]_{ijkl} + \sum_{q=1}^{N_1} w(B^q) \sum_{p=1}^{2} 4[F(B_p^q)]_{ijkl} + \sum_{q=1}^{N_2} w(C^q) \sum_{p=1}^{24} [F(C_p^q)]_{ijkl} + \sum_{q=1}^{N_2} w(D^q) \sum_{p=1}^{48} [F(D_p^q)]_{ijkl} \}. \quad (23)$$

In this equation, A^1, B^1, B, C, D, N_1 and N_2 are parameters of the Lebedev quadrature. Depending on order, some of these parameters can be zero, resulting in a more efficient evaluation.

Remark 3. In the micro-mechanical model discussed in Section 2, the (internal) variables are stored in the memory of the random-access memory of the computer. For usage on only the micro-mechanical model, this is a computationally efficient approach because the amount of stored data is low. On the other hand, for the coupled multi-scale model, this approach to store data becomes unfeasible (at least for a

Table 1
Constitutive properties of the matrix and reinforcements of the polyamide/glass SFRC.

	Fibers		Matrix					
Parameter	E_f (GPa)	ν_f (-)	E_m (GPa)	ν_m (-)	σ_y (MPa)	K (MPa)	R_∞ (MPa)	m (-)
Value	76	0.22	3.1	0.35	25	150	20	325

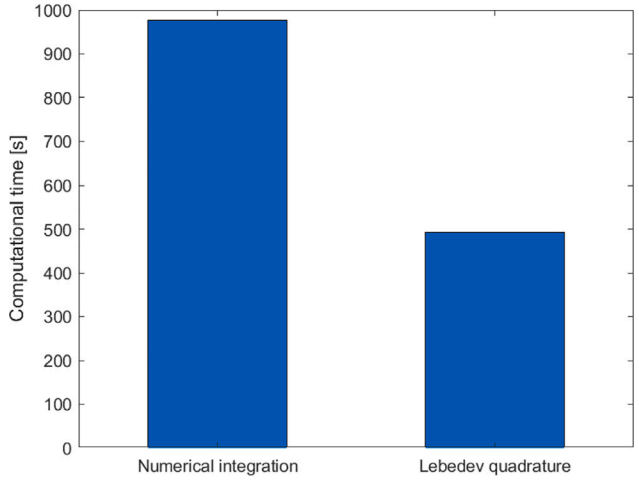

Fig. 12. Comparison of computational time for the numerical evaluation and the Lebedev quadrature of the Eshelby tensor.

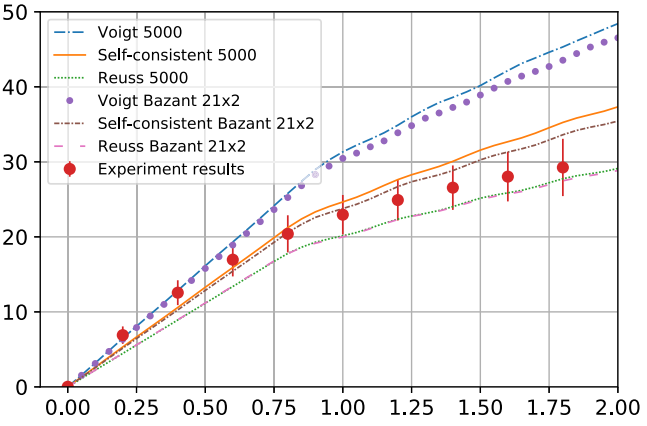

Fig. 13. Stress–strain curves obtained from the coupled multi-scale model, and experimental results taken from [34].

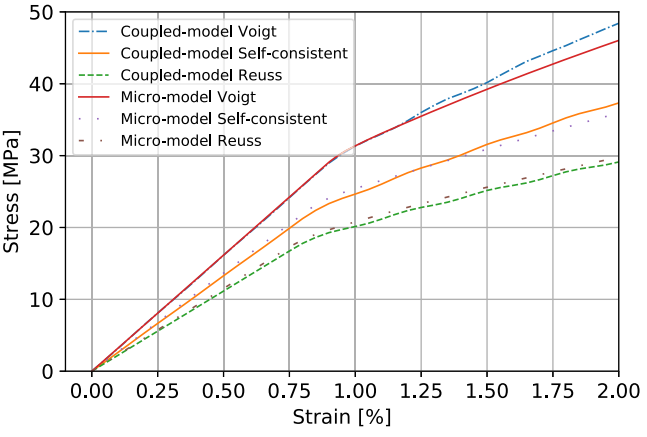

Fig. 14. A comparison of the stress–strain curves obtained from the coupled multi-scale model and the micro-mechanical model.

Table 2
Material properties used for the polyamide/glass SFRC.

Material property	Value
Volume fraction μ	0.22
Young's modulus E	3.85 [GPa]
Poisson's ratio ν	0.34
k	1.93
R_y	6.52
σ_{y0}	33.03 [MPa]
H_1	493.52
H_2	15.00
H_3	10.07

personal computer) due to the large amount of data. To clarify, the internal variables for each UC are (i): The accumulated plastic strain (a scalar value for each UC), (ii): The UC specific local tangent stiffness tensor (a 6×6 matrix in Voigt form for each UC), (iii): The stress tensor for each UC (a 6×1 matrix in Voigt form), (iv): The strain tensor (a 6×1 matrix for each UC). Thus, a huge amount data should be stored. In this work, a different strategy for handling these data is adopted. A text file is created on the computer hard drive and the data is stored in the file. In the micro-mechanical model, at the start, the file is read and the variables are temporarily saved in memory. During the calculations in the micro-mechanical model, internal variables are changed and at the end, before the resulting stress is returned to the macroscale, these variables are saved to the text file. Then, the same procedure is followed for the next integration point.

5. Results and discussion

This section presents the results obtained from the coupled multi-scale model. In addition, the effects of the adopted techniques with the purpose to lower the computational cost of the model are investigated. Also, comparisons to experimental results are conducted. Two different SFRCs are used in the numerical examples, **(i):** Polyamide matrix reinforced with short glass fibers, and **(ii):** Polypropylene matrix reinforced with short flax fibers. In the polyamide/glass composite, glass fibers are considered elastic and matrix material is elastoplastic and follows J_2 plasticity with isotropic linear–exponential hardening:

$$R(\bar{\varepsilon}^p) = K\bar{\varepsilon}^p + R_\infty \left[1 - \exp(-m\bar{\varepsilon}^p)\right], \tag{24}$$

where $\bar{\varepsilon}^p$ is accumulated plastic strain, K, R_∞ and m are material parameters. The matrix and reinforcements constitutive properties are given Table 1 (see more details in [20,35]).

As a result, the parameters for the surrogate model for each composite is given in Table 2 and Table 4, respectively. For the polyamide/glass SFRC, Mirkhalaf et al. [20] showed that the proposed UC is representing the response of the unidirectional composite well. It is however recommended, for a generic SFRC with arbitrary matrix and fiber, to use a unidirectional RVE so that the interactions between fibers are taken into account, and the representativeness of the results is assured.

To obtain a representative number of UCs for simulations of the polyamide/glass SFRC, a sensitivity analysis is conducted. Fig. 7 shows the deviation in the Young's modulus for different number of random orientated UCs (fibers). Considering the obtained results, a number of 5000 fibers is considered for the micro-mechanical simulations of the polyamide/glass SFRC. A maximum strain of 1.75% is applied in 175 increments. Fig. 8 shows the obtained stress–strain curves using

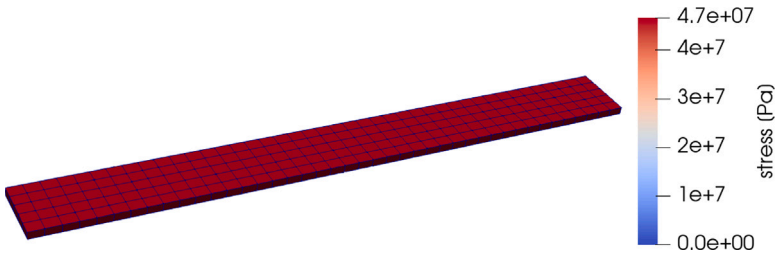

Fig. 15. Contour plot of the stress distribution (in the loading direction) in the FE model.

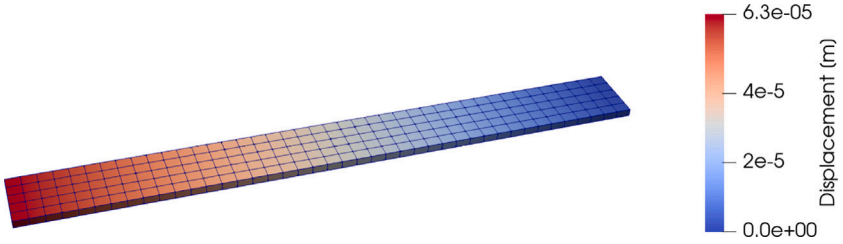

Fig. 16. Contour plot of the displacement field in the FE model.

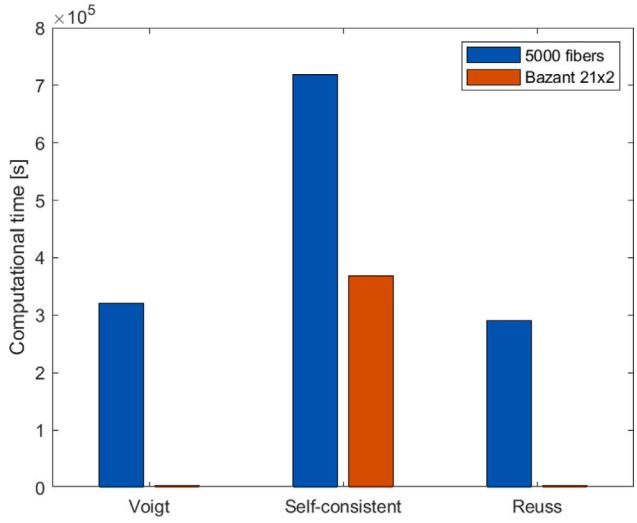

Fig. 17. Computational time of the coupled model for 5000 random fibers and Bazant 21 × 2 scheme with the Voigt, self-consistent and Reuss interaction.

different interaction assumptions. As expected, the Voigt and Reuss interactions give the upper and lower bound of the stress–strain response, respectively and the self-consistent response is obtained between the two bounds.

5.1. Different integration schemes for orientation distribution

A comparison is then made between different integration schemes for incorporating the effect of the orientation distributions, i.e. trapezoidal integration and the Bazant schemes. Fig. 9 shows a comparison between the obtained stress–strain curves for (a) the Voigt interaction, (b) the self-consistent interaction and (c) the Reuss interaction. The figure shows that the results obtained using the Bazant schemes are in a good agreement with those obtained using the trapezoidal integration (to be considered as a reference case). The main advantage from using the Bazant schemes is, however, the considerable decrease in computational effort. Fig. 10 shows the computational time for the three considered interactions with the three different orientation methods. It is seen that using the Bazant schemes results in a remarkable improvement in terms of computational time, specially for the Voigt and Reuss interactions. Also, for the self-consistent interaction, the computational time has been reduced using the Bazant schemes. It should, however, be noted that for this example the calculations of the Eshelby tensor is still carried out using the original numerical integration scheme presented in Section 4.2.

5.2. Different integration schemes for calculation of the Eshelby tensor

A comparison is also performed between the trapezoidal and Lebedev integration schemes for the calculation of the Eshelby tensor. As before, the polyamide/glass SFRC is considered for this comparison. The 15th order Lebedev quadrature is used which has 86 points on the unit sphere. For computing the volume averaging considering the fiber orientation distribution, the Bazant 21 × 2 scheme is used for both simulations.

Fig. 11 shows a comparison between the obtained stress–strain curves using the two integration schemes. It should be noted that a higher order quadrature will result in more accurate results, however, at the expense of an increasing computational cost. Fig. 12 shows the calculation times for the two approaches for obtaining the Eshelby tensor. It is seen that the Lebedev quadrature reduces the computational burden of the model by approximately 50%.

5.3. Comparison to experimental results

Comparisons to experimental results are also conducted. Coupled multi-scale simulations are carried out for the polypropylene/flax SFRC, and the obtained results are compared to experimental results taken from [34]. Based on Modniks and Andersons [34,43], micro-graphs of cross-sections of the composites showed the fiber orientation distribution was reasonably random. Hence, 3D random distribution of fibers is considered in the simulations.

Flax fibers are considered elastic, and the polypropylene matrix is modeled as an elasto-plastic material using the Ramberg–Osgood model. In a uniaxial loading condition, stress and strain are related by [34]:

$$\varepsilon = \frac{\sigma}{E}\left(1 + a\left(\frac{\sigma}{\sigma_0}\right)^{n-1}\right), \tag{25}$$

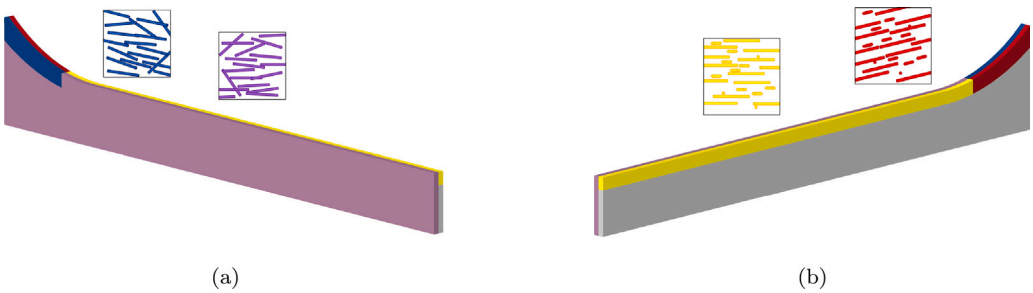

Fig. 18. FE mesh with fibers orientation highlighted: (a) the 'backside' of the FE mesh with in purple the fibers aligned along the backside (in-plane) and in blue rotated with 15 degrees (to compensate the radius in the sample), (b) the 'front side' of the FE mesh with in yellow the fibers aligned with the top surface (out-of-plane), in red turned 15 degrees and in black the fibers orientated via the Bazant 21 × 2 scheme.

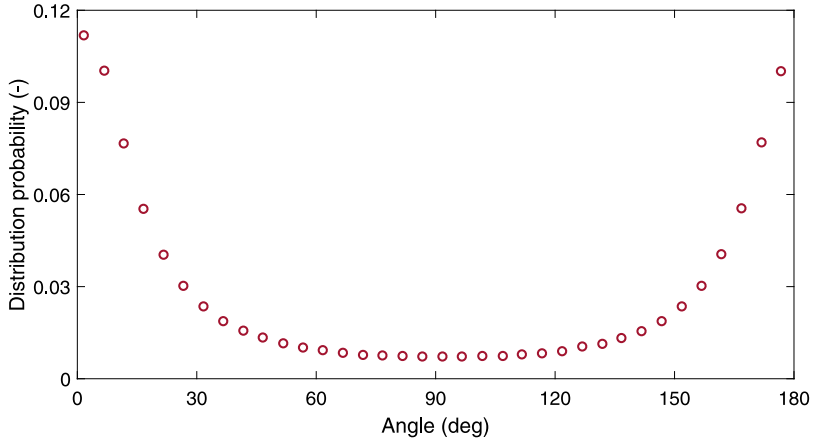

Fig. 19. Planar and preferentially oriented distribution of fibers of the polyamide/glass SFRC taken from [20] reproduced after [35].

Table 3
Constitutive properties of the matrix and reinforcements of the polypropylene/flax SFRC [34].

	Fibers		Matrix				
Parameter	E_f (GPa)	ν_f (-)	E_m (GPa)	ν_m (-)	σ_0 (MPa)	a (-)	n (-)
Value	69	0.15	1.6	0.4	16	0.235	5.44

Table 4
Material properties for polypropylene/flax SFRC, taken from [20].

Material property	Value
Volume fraction μ	0.13
Young's modulus E	1.99 [GPa]
Poisson's ratio ν	0.39
k	2.77
R_y	47.74
σ_{y0}	19.98 [MPa]
H_1	131.16
H_2	11.97
H_3	10.04

where, E is the Young's modulus and a, σ_0 and n are the model parameters. The constitutive properties of the matrix and reinforcements are given in Table 3 (see more details in [34]). As mentioned above, the material parameters, for the surrogate constitutive model, are taken from [20] and given in Table 4. The macroscopic sample dimensions are taken from [36], and the FE model shown in Fig. 4 is used. Furthermore, a macroscopic strain of maximum 2% is applied in 40 load increments.

The obtained stress–strain figures from the coupled multi-scale model are shown in Fig. 13 together with experimental results taken from [34]. It is seen that the self-consistent results match reasonably well with the experimental results, even though the stress is slightly overestimated in the non-linear regime. This is however in line with the micro-mechanical simulations, and as pointed out by Mirkhalaf et al. [20], the assumption of matrix-fiber *perfect* bonding is probably not completely realistic for this material.

In the non-linear regime, fluctuations are seen for all three considered interaction assumptions. These fluctuations are due to using an explicit solver in combination with relatively large load (increment) steps. The explicit solver is an approximate solution algorithm and is, in the non-linear regime, sensitive to load steps.

Fig. 14 shows a comparison between the results obtained from the coupled multi-scale model and the results from the micro-mechanical model. The observed small difference between the predictions of the two models is due to different orientations i.e., the utilized 5000 fiber orientations are randomly created distributions and are not exactly the same for all simulations. The contour plot of the stress and deformation distributions in the FE model are shown in Fig. 15 and 16, respectively. It should also be mentioned that the plastic strain of all UCs are also stored and can be accessed during and at the end of simulation. The computational time of all the coupled simulations are shown in Fig. 17. It is seen that the adopted strategies and techniques for improving the computational efficiency of the model remarkably reduced the computational cost of the model, in particular for the Voigt and Reuss interactions. The computational efficiency is reduced by 99%, 48.6% and 98.9% for the Voigt, self-consistent and Reuss interactions, respectively.

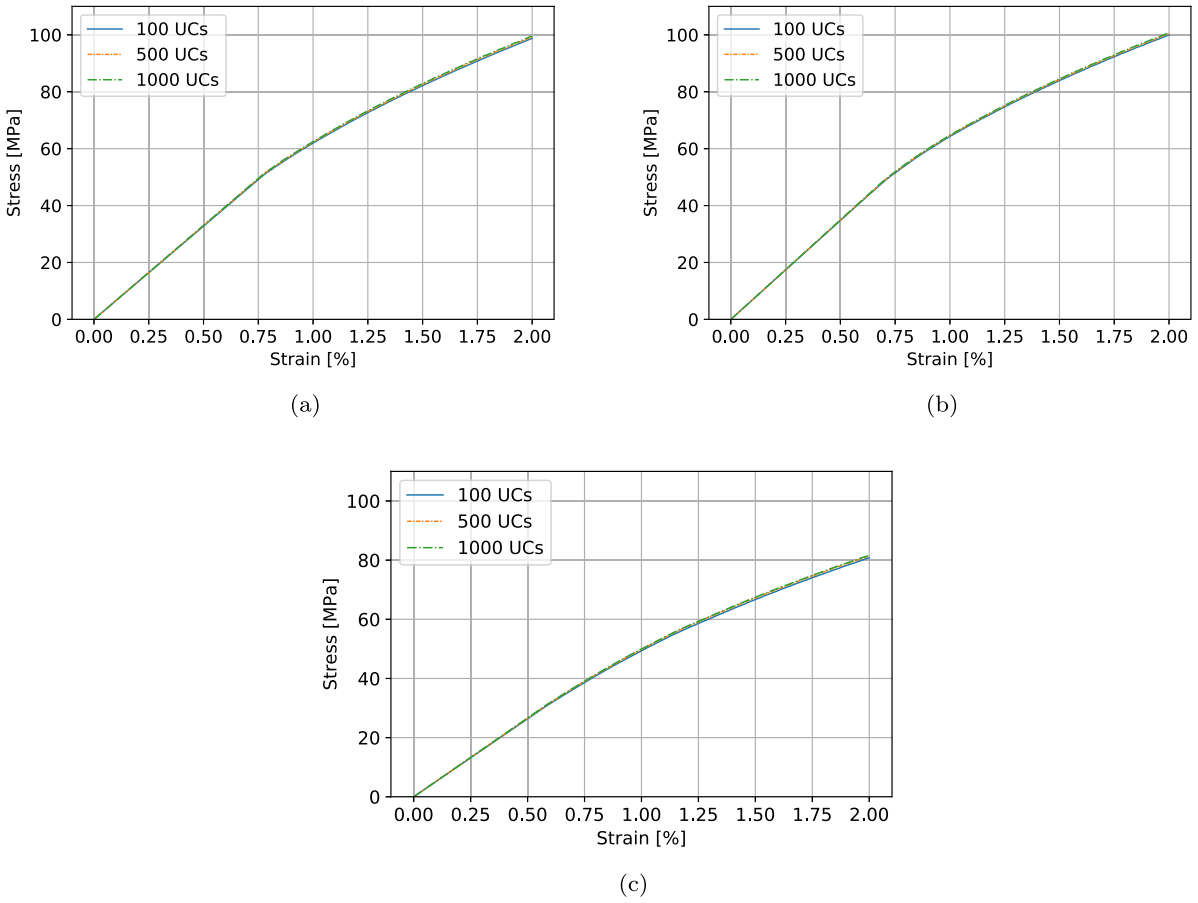

Fig. 20. Comparison of the non-linear elastoplastic stress–strain curve with the planar and preferentially orientated distributed fibers and considering different amount of UCs. The stress–strain curves are obtained with the coupled model on a single 3D 8 integration point element. (a) Voigt interaction. (b) Self-consistent interaction. (c) Reuss interaction. The graphs show clearly that the predictions have very small influence of the number of UCs.

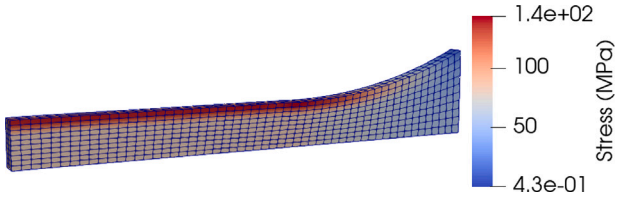

Fig. 21. Contour plot of the stress distribution (in the loading direction) in the FE model with the Voigt interaction.

5.4. Coupled simulations with a varying fiber orientation distribution

To showcase the capabilities of the multi-scale model to account for a macroscopically varying fiber orientation distribution, a fictitious injection molded dog-bone-shaped specimen is simulated. A Polyamide/glass SFRC is considered for the coupled simulations (see Table 2 for material properties). The injection flow is considered in the longitudinal direction. Thereby, it is assumed that along the surface, fibers are aligned with the flow direction and in the core of the specimen, orientation of fibers is assumed to be completely random.

Due to existing symmetries, again only one eighth of the sample is simulated. The sample is spatially discretized with 1100 3D elements with 8 integration points. Fig. 18 shows the used FE mesh with the different fiber orientations at different parts of the specimen. The 'backside' of the sample is the outer layer which corresponds with the skin layer and the fibers are aligned with the flow direction (in-plane). The inner layer is the 'front side' in the sample which corresponds with the core, where close to the surface, the fibers are aligned with the flow (out-of-plane) and away from the surface, the fibers are randomly distributed. Points close to the surface are described with a planar preferentially orientated distribution following [20], reproduced after [35]. Fig. 19 shows the preferentially planar orientation distribution of fibers.

For the preferential orientation distribution, first, a sensitivity analysis is conducted to assess the dependency of the coupled model to the number of UCs (considered with the trapezoidal integration scheme) using a single 3D element with 8 integration points. Fig. 20 shows the obtained stress–strain curves using different interaction assumptions. Since the amount of UCs have a very small influence, 100 UCs are considered to be sufficient (for the elements with planar preferential orientation) for the coupled simulations of the dog-bone specimen. It should be emphasized that for other SFRCs with different matrix/reinforcements and/or different orientation distributions, a considerable dependency on the number of UCs might be observed and hence, an independent sensitivity analysis should be conducted to obtain a representative number of UCs.

The elements in the core layer are considered with random 3D orientations and are modeled with the Bazant 21 × 2 scheme (at the micro level).

A macroscopic strain of 2% is applied in 40 load increments. The contour plot of the stress (in the loading direction) in the FE model is shown in Fig. 21. The figure shows a stress concentration in the elements where the fibers are aligned in the loading direction, which is expected.

6. Concluding remarks

Parts fabricated from short fiber reinforced composites typically posses different fiber orientations at different points. To analyze the mechanical performance of such parts, a multi-scale model is needed where the micro-structural characteristics are considered at the sub-scale level. Therefore, in this study, a coupled multi-scale model was developed to predict the elasto-plastic behavior of these materials. The Finite Element Method was used at the macro-level and an orientation averaging micro-mechanical model was used at the micro-level. Further, the macroscopic FE equations were solved using an explicit time-stepping algorithm.

At the micro-level, three different global–local interactions namely, Voigt, Reuss and self-consistent assumptions were used. As expected, the multi-scale model showed to be computationally expensive. In order to reduce the computational burden of the model, the originally used trapezoidal integration schemes were replaced by more efficient integration approaches. The Bazant integration scheme was used for random orientation distributions and the Lebedev integration approach was used for the calculation of the Eshelby tensor. The results show that there is a substantial computational speed-up if these more efficient integration schemes are adopted. In fact, the modified model, in which the two efficient integration procedures are adopted, showed a remarkably improved computational efficiency, particularly for the Voigt and Reuss interactions which have been improved by 99% and 98.8%, respectively. The self-consistent interaction is improved by 48.6%.

In conclusion, this model enables full-scale analysis of real-life structures, fabricated from SFRCs, in a computationally feasible manner. It is also emphasized that a variety of fiber orientation distributions (as observed in actual injection molded SFRC parts) can be conveniently accommodated by the proposed model.

CRediT authorship contribution statement

B.A. Castricum: Methodology, Software, Validation, Formal analysis, Investigation, Data curation, Visualization, Writing – original draft, Writing – review & editing. **M. Fagerström:** Conceptualization, Methodology, Writing – review & editing, Supervision, Funding acquisition. **M. Ekh:** Conceptualization, Methodology, Writing – review & editing. **F. Larsson:** Conceptualization, Methodology, Writing – review & editing, Supervision. **S.M. Mirkhalaf:** Conceptualization, Methodology, Writing – original draft, Writing – review & editing, Supervision, Project administration, Funding acquisition.

Declaration of competing interest

The authors declare that they have no known competing financial interests or personal relationships that could have appeared to influence the work reported in this paper.

Data availability

Data will be made available on request.

Acknowledgments

B.A. Castricum acknowledges financial support from the Erasmus+ programme of the European Union. M. Ekh acknowledges financial support from the Swedish Research Council (VR grant: 2018-06482). M. Fagerström gratefully acknowledges the support through Vinnova's strategic innovation programme LIGHTer, Sweden and the support from Materials Science Area of Advance at Chalmers University of Technology, Sweden. S.M. Mirkhalaf is grateful for the financial support from the Swedish Research Council (VR grant: 2019-04715) and the University of Gothenburg, Sweden.

References

[1] Kammoun S, Doghri I, Brassart L, Delannay L. Micromechanical modeling of the progressive failure in short glass–fiber reinforced thermoplastics – First Pseudo-Grain Damage model. Composites A 2015;73:166–75. http://dx.doi.org/10.1016/j.compositesa.2015.02.017, URL http://www.sciencedirect.com/science/article/pii/S1359835X1500069X.

[2] Ishikawa Takashi, Amaoka Kazuaki, Masubuchi Yuichi, Yamamoto Tetsuya, Yamanaka Atsuhiko, Arai Masahiro, Takahashi Jun. Overview of automotive structural composites technology developments in Japan. Compos Sci Technol 2018;155:221–46. http://dx.doi.org/10.1016/j.compscitech.2017.09.015, URL http://www.sciencedirect.com/science/article/pii/S0266353817316202.

[3] Rezaei F, Yunus R, Ibrahim NA, Mahdi ES. Development of short-carbon-fiber-reinforced polypropylene composite for car bonnet. Polym-Plast Technol Eng 2008;47(4):351–7. http://dx.doi.org/10.1080/03602550801897323.

[4] Mirkhalaf SM, Eggels EH, Anantharanga AT, Larsson F, Fagerström M. Short fiber composites: Computational homogenization vs orientation averaging. In: ICCM22 2019. Engineers Australia; 2019, p. 3000.

[5] Mirkhalaf SM, Eggels EH, van Beurden TJH, Larsson F, Fagerström M. A finite element based orientation averaging method for predicting elastic properties of short fiber reinforced composites. Composites B 2020;202:108388. http://dx.doi.org/10.1016/j.compositesb.2020.108388, URL http://www.sciencedirect.com/science/article/pii/S1359836820334363.

[6] Eshelby JD. He determination of the elastic field of an ellipsoidal inclusion, and related problems.. Proc R Soc Lond Ser A 1957;241(1226):376–96, URL http://micro.stanford.edu/caiwei/me340b/content/me340b-notes_v01.pdf.

[7] Hashin Z, Shtrikman S. On some variational principles in anisotropic and nonhomogeneous elasticity. J Mech Phys Solids 1962;10(4):335–42. http://dx.doi.org/10.1016/0022-5096(62)90004-2, URL https://www.sciencedirect.com/science/article/pii/0022509662900042.

[8] Hashin Z, Shtrikman S. A variational approach to the theory of the elastic behaviour of multiphase materials. J Mech Phys Solids 1963;11(2):127–40. http://dx.doi.org/10.1016/0022-5096(63)90060-7, URL https://www.sciencedirect.com/science/article/pii/0022509663900607.

[9] Hill R. A self-consistent mechanics of composite materials. J Mech Phys Solids 1965;13(4):213–22. http://dx.doi.org/10.1016/0022-5096(65)90010-4, URL https://www.sciencedirect.com/science/article/pii/0022509665900104.

[10] Budiansky B. On the elastic moduli of some heterogeneous materials. J Mech Phys Solids 1965;13(4):223–7. http://dx.doi.org/10.1016/0022-5096(65)90011-6, URL https://www.sciencedirect.com/science/article/pii/0022509665900116.

[11] Mori T, Tanaka K. Average stress in matrix and average elastic energy of materials with misfitting inclusions. Acta Metall 1973;21(5):571–4. http://dx.doi.org/10.1016/0001-6160(73)90064-3, URL http://www.sciencedirect.com/science/article/pii/0001616073900643.

[12] Tian Wenlong, Qi Lehua, Zhou Jiming, Liang Junhao, Ma Yuqin. Representative volume element for composites reinforced by spatially randomly distributed discontinuous fibers and its applications. Compos Struct 2015;131:366–73. http://dx.doi.org/10.1016/j.compstruct.2015.05.014.

[13] Qi Lehua, Tian Wenlong, Zhou Jiming. Numerical evaluation of effective elastic properties of composites reinforced by spatially randomly distributed short fibers with certain aspect ratio vol. 131. 2015, p. 843–51.

[14] Tikarrouchine E, Chatzigeorgiou G, Praud F, Piotrowski B, Chemisky Y, Meraghni F. Three-dimensional FE2method for the simulation of non-linear, rate-dependent response of composite structures. Compos Struct 2018;193(March):165–79. http://dx.doi.org/10.1016/j.compstruct.2018.03.072.

[15] Mirkhalaf M, Ashrafi B. A numerical study on improving the specific properties of staggered composites by incorporating voids. Mater. Today Commun. 2017;13:144–54. http://dx.doi.org/10.1016/j.mtcomm.2017.09.011, URL http://www.sciencedirect.com/science/article/pii/S2352492817302210.

[16] Spahn J, Andrä H, Kabel M, Müller R. A multiscale approach for modeling progressive damage of composite materials using fast Fourier transforms. Comput Methods Appl Mech Engrg 2014;268:871–83. http://dx.doi.org/10.1016/j.cma.2013.10.017, URL https://www.sciencedirect.com/science/article/pii/S0045782513002697.

[17] Schneider M, Ospald F, Kabel M. Computational homogenization of elasticity on a staggered grid. Internat J Numer Methods Engrg 2016;105(9):693–720. http://dx.doi.org/10.1002/nme.5008, URL https://www.scopus.com/inward/record.uri?eid=2-s2.0-84956592567&doi=10.1002%2fnme.5008&partnerID=40&md5=16db522cfcc01c880eaceda600136491 cited By 86.

[18] Doghri I, Brassart L, Adam L, Gérard JS. A second-moment incremental formulation for the mean-field homogenization of elasto-plastic composites. Int J Plast 2011;27(3):352–71. http://dx.doi.org/10.1016/j.ijplas.2010.06.004.

[19] Heidari-Rarani M, Bashandeh-Khodaei-Naeini K, Mirkhalaf SM. Micromechanical modeling of the mechanical behavior of unidirectional composites – A comparative study. J Reinf Plast Compos 2018;37(16):1051–71, URL https://www.scopus.com/inward/record.uri?eid=2-s2.0-85047661544&doi=10.1177%2f0731684418779441&partnerID=40&md5=4c75382ab5584933e8451d6e0efb2e91.

[20] Mirkhalaf SM, van Beurden TJH, Ekh M, Larsson F, Fagerström M. An FE-based orientation averaging model for elasto-plastic behavior of short fiber composites. Int J Mech Sci 2022;219:107097. http://dx.doi.org/10.1016/j.ijmecsci.2022.107097, URL https://www.sciencedirect.com/science/article/pii/S0020740322000339.

[21] Mirkhalaf M, van Dommelen JAW, Govaert LE, Furmanski J, Geers MGD. Micromechanical modeling of anisotropic behavior of oriented semicrystalline polymers. J Polym Sci B 2019;57(7):378–91. http://dx.doi.org/10.1002/polb.24791, URL https://www.scopus.com/inward/record.uri?eid=2-s2.0-85061446380&doi=10.1002%2fpolb.24791&partnerID=40&md5=57d95ad08cec471aa9afc82a3124f70c.

[22] Mirkhalaf SM, Pires FM Andrade, Simoes R. Determination of the size of the representative volume element (RVE) for the simulation of heterogeneous polymers at finite strains. Finite Elem Anal Des 2016;119:30–44. http://dx.doi.org/10.1016/j.finel.2016.05.004, URL http://www.sciencedirect.com/science/article/pii/S0168874X16300750.

[23] Svenning E, Larsson F, Fagerström M. A two-scale modeling framework for strain localization in solids: Xfem procedures and computational aspects. Comput Struct 2019;211:43–54. http://dx.doi.org/10.1016/j.compstruc.2018.08.003, URL https://www.scopus.com/inward/record.uri?eid=2-s2.0-85055746239&doi=10.1016%2fj.compstruc.2018.08.003&partnerID=40&md5=ea589ea2f68e148be141c58ea2760654.

[24] van Bree SEHM, Rokoš O, Peerlings RHJ, Doškář M, Geers MGD. A Newton solver for micromorphic computational homogenization enabling multiscale buckling analysis of pattern-transforming metamaterials. Comput Methods Appl Mech Engrg 2020;372. http://dx.doi.org/10.1016/j.cma.2020.113333, URL https://www.scopus.com/inward/record.uri?eid=2-s2.0-85090117223&doi=10.1016%2fj.cma.2020.113333&partnerID=40&md5=33863ba6aadd7ab856770750ce1aff88.

[25] Lopes IAR, Pires FMA, Reis FJP. A mixed parallel strategy for the solution of coupled multi-scale problems at finite strains. Comput Mech 2018;61(1–2):157–80. http://dx.doi.org/10.1007/s00466-017-1472-6, URL https://www.scopus.com/inward/record.uri?eid=2-s2.0-85029543437&doi=10.1007%2fs00466-017-1472-6&partnerID=40&md5=25a92ba5bb65a446b8e511a975c3f45e.

[26] Gupta Mahesh, Wang KK. Fiber orientation and mechanical properties of short-fiber-reinforced injection-molded composites: Simulated and experimental results. Polym Compos 1993;14(5):367–82. http://dx.doi.org/10.1002/pc.750140503, arXiv:https://onlinelibrary.wiley.com/doi/pdf/10.1002/pc.750140503.

[27] Zaidani Mouna, Omar Mohammad A, Kumar S. Coupling of injection molding process to mechanical properties of short fiber composites: A through process modeling approach. J Reinf Plast Compos 2015;34(23):1963–78. http://dx.doi.org/10.1177/0731684415609138.

[28] de Borst René, Crisfield Mike A, Remmers Joris JC, Verhoosel Clemens V. Non-linear finite element analysis. Non-Linear Finite Element Analysis of Solids and Structures. John Wiley & Sons, Ltd; 2012, p. 31–62. http://dx.doi.org/10.1002/9781118375938.ch2.

[29] Bažant P, Oh BH. Efficient numerical integration on the surface of a sphere. ZAMM - J Appl Math Mech 1986;66(1):37–49. http://dx.doi.org/10.1002/zamm.19860660108.

[30] Qu Mengmeng, Jiang Dazhi, Lu Lucy X. An optimal scheme for numerical evaluation of Eshelby tensors and its implementation in a MATLAB package for simulating the motion of viscous ellipsoids in slow flows. Comput Geosci 2016;96:98–108. http://dx.doi.org/10.1016/j.cageo.2016.08.005.

[31] Advani Suresh G, Tucker Charles L. The use of tensors to describe and predict fiber orientation in short fiber composites. J Rheol 1987;31(8):751–84. http://dx.doi.org/10.1122/1.549945.

[32] Dafalias YF, Rashid MM. The effect of plastic spin on anisotropic material behavior. Int J Plast 1989;5(3):227–46.

[33] Aravas N. Finite elastoplastic transformations of transversely isotropic metals. Int J Solids Struct 1992;29(17):2137–57.

[34] Modniks J, Andersons J. Modeling the non-linear deformation of a short-flax-fiber-reinforced polymer composite by orientation averaging. Composites B 2013;54(1):188–93. http://dx.doi.org/10.1016/j.compositesb.2013.04.058.

[35] Kammoun S, Doghri I, Adam L, Robert G, Delannay L. First pseudo-grain failure model for inelastic composites with misaligned short fibers. Composites A 2011;42(12):1892–902. http://dx.doi.org/10.1016/j.compositesa.2011.08.013, URL http://www.sciencedirect.com/science/article/pii/S1359835X11002739.

[36] Andersons J, Spārniš E, Joffe R. Stiffness and strength of flax fiber/polymer matrix composites. Polym Compos 2006;27(2):221–9. http://dx.doi.org/10.1002/pc.20184, URL http://doi.wiley.com/10.1002/pc.20184.

[37] Hou Chieh, Ateshian Gerard A. Computer methods in biomechanics and biomedical engineering A Gauss-Kronrod-Trapezoidal integration scheme for modeling biological tissues with continuous fiber distributions a Gauss-Kronrod-Trapezoidal integration scheme for modeling biological tissues with continuous fiber distributions. Comput Methods Biomech Biomed Eng 2016;19(8):883–93. http://dx.doi.org/10.1080/10255842.2015.1075518, URL https://www.tandfonline.com/action/journalInformation?journalCode=gcmb20http://dx.

[38] Itskov Mikhail. On the accuracy of numerical integration over the unit sphere applied to full network models. Comput Mech 2016;57(5):859–65. http://dx.doi.org/10.1007/s00466-016-1265-3.

[39] Levasseur S, Collin F, Charlier R, Kondo D. On micromechanical damage modeling in geomechanics: Influence of numerical integration scheme. J Comput Appl Math 2013;246:215–24. http://dx.doi.org/10.1016/j.cam.2012.05.022.

[40] Larijani Nasim, Johansson Göran, Ekh Magnus. Hybrid micro-macromechanical modeling of anisotropy evolution in pearlitic steel. Eur J Mech A/Solids 2013;38:38–47. http://dx.doi.org/10.1016/j.euromechsol.2012.09.011.

[41] Lebedev VI. Quadratures on a sphere. USSR Comput Math Math Phys 1976;16(2):10–24. http://dx.doi.org/10.1016/0041-5553(76)90100-2.

[42] Lebensohn RA, Tomé CN, Maudlin PJ. A selfconsistent formulation for the prediction of the anisotropic behavior of viscoplastic polycrystals with voids. J Mech Phys Solids 2004;52(2):249–78. http://dx.doi.org/10.1016/S0022-5096(03)00114-5.

[43] Modniks J, Andersons J. Modeling elastic properties of short flax fiber-reinforced composites by orientation averaging. Comput Mater Sci 2010;50(2):595–9. http://dx.doi.org/10.1016/j.commatsci.2010.09.022.